

Deeply virtual Compton scattering off the neutron

M. Benali^{1,2*}, C. Desnault³, M. Mazouz¹, Z. Ahmed⁴, H. Albataineh⁵, K. Allada⁶, K. A. Aniol⁷, V. Bellini⁸, W. Boeglin⁹, P. Bertin^{2,10}, M. Brossard², A. Camsonne¹⁰, M. Canan¹¹, S. Chandavar¹², C. Chen¹³, J.-P. Chen¹⁰, M. Defurne¹⁴, C. W. de Jager^{10,42}, R. de Leo¹⁵, A. Deur¹⁰, L. El Fassi^{16,17}, R. Ent¹⁰, D. Flay¹⁸, M. Friend¹⁹, E. Fuchey², S. Frullani^{20,42}, F. Garibaldi²⁰, D. Gaskell¹⁰, A. Giusa⁸, O. Glamazdin²¹, S. Golge²², J. Gomez¹⁰, O. Hansen¹⁰, D. Higinbotham¹⁰, T. Holmstrom²³, T. Horn²⁴, J. Huang¹⁰, M. Huang²⁵, G. M. Huber²⁶, C. E. Hyde^{2,11}, S. Iqbal⁷, F. Itard², Ho. Kang²⁷, Hy. Kang²⁷, A. Kelleher²⁸, C. Keppel¹⁰, S. Koirala¹¹, I. Korover²⁹, J. J. LeRose¹⁰, R. Lindgren³⁰, E. Long¹⁰, M. Magne², J. Mammei³², D. J. Margaziotis⁷, P. Markowitz⁹, A. Martí Jiménez-Argüello^{3,33}, F. Meddi²⁰, D. Meekins¹⁰, R. Michaels¹⁰, M. Mihovilovic³⁴, N. Muangma⁶, C. Muñoz Camacho^{2,3}, P. Nadel-Turonski¹⁰, N. Nuruzzaman¹³, R. Paremuzyan³, R. Pomatsalyuk²¹, A. Puckett¹⁰, V. Punjabi³⁶, Y. Qiang¹⁰, A. Rakhman⁴, M. N. H. Rashad¹¹, S. Riordan¹⁰, J. Roche¹², G. Russo⁸, F. Sabatié¹⁴, K. Saenboonruang^{30,38}, A. Saha^{10,42}, B. Sawatzky^{10,18}, L. Selvy³¹, A. Shahinyan³⁹, S. Sirca³⁴, P. Solvignon^{10,42}, M. L. Sperduto⁸, R. Subedi⁴⁰, V. Sulcosky⁶, C. Sutera⁸, W. A. Tobias³⁰, G. M. Urciuoli⁴¹, D. Wang³⁰, B. Wojtsekhowski¹⁰, H. Yao¹⁰, Z. Ye¹⁰, L. Zana⁴, X. Zhan³⁷, J. Zhang¹⁰, B. Zhao²⁸, Z. Zhao³⁰, X. Zheng³⁰ and P. Zhu³⁰

The three-dimensional structure of nucleons (protons and neutrons) is embedded in so-called generalized parton distributions, which are accessible from deeply virtual Compton scattering. In this process, a high-energy electron is scattered off a nucleon by exchanging a virtual photon. Then, a highly energetic real photon is emitted from one of the quarks inside the nucleon, which carries information on the quark's transverse position and longitudinal momentum. By measuring the cross-section of deeply virtual Compton scattering, Compton form factors related to the generalized parton distributions can be extracted. Here, we report the observation of unpolarized deeply virtual Compton scattering off a deuterium target. From the measured photon-electroproduction cross-sections, we have extracted the cross-section of a quasifree neutron and a coherent deuteron. Due to the approximate isospin symmetry of quantum chromodynamics, we can determine the contributions from the different quark flavours to the helicity-conserved Compton form factors by combining our measurements with previous ones probing the proton's internal structure. These results advance our understanding of the description of the nucleon structure, which is important to solve the proton spin puzzle.

Understanding the quark and gluon structure of the nucleon is one of the outstanding challenges in hadronic physics. For decades, elastic and deep inelastic (DIS) lepton–nucleon scattering have been investigated to obtain information on the transverse spatial distribution of partons¹, encoded by the nucleon

form factors (FFs), and their longitudinal momentum distribution, characterized by parton distribution functions (PDFs)². The longitudinal direction is given by the momentum of the virtual photon mediating the interaction. By unifying FFs and PDFs, the theoretical framework of generalized parton distributions (GPDs)^{3,4}

¹Faculté des Sciences de Monastir, Monastir, Tunisia. ²Clermont Université, Université Blaise Pascal, CNRS/IN2P3, Laboratoire de Physique Corpusculaire, Clermont-Ferrand, France. ³Institut de Physique Nucléaire CNRS-IN2P3, Orsay, France. ⁴Syracuse University, Syracuse, NY, USA. ⁵Texas A&M University—Kingsville, Kingsville, TX, USA. ⁶Massachusetts Institute of Technology, Cambridge, MA, USA. ⁷California State University, Los Angeles, Los Angeles, CA, USA. ⁸INFN/Sezione di Catania, Catania, Italy. ⁹Florida International University, Miami, FL, USA. ¹⁰Thomas Jefferson National Accelerator Facility, Newport News, VA, USA. ¹¹Old Dominion University, Norfolk, VA, USA. ¹²Ohio University, Athens, OH, USA. ¹³Hampton University, Hampton, VA, USA. ¹⁴Irfu, CEA, Université Paris—Saclay, Gif-sur-Yvette, France. ¹⁵Università di Bari, Bari, Italy. ¹⁶Rutgers, The State University of New Jersey, Piscataway, NJ, USA. ¹⁷Mississippi State University, Mississippi State, MS, USA. ¹⁸Temple University, Philadelphia, PA, USA. ¹⁹Carnegie Mellon University, Pittsburgh, PA, USA. ²⁰INFN/Sezione Sanità, Roma, Italy. ²¹Kharkov Institute of Physics and Technology, Kharkov, Ukraine. ²²North Carolina Central University, Durham, NC, USA. ²³Longwood University, Farmville, VA, USA. ²⁴The Catholic University of America, Washington, DC, USA. ²⁵Duke University, Durham, NC, USA. ²⁶University of Regina, Regina, Saskatchewan, Canada. ²⁷Seoul National University, Seoul, South Korea. ²⁸College of William and Mary, Williamsburg, VA, USA. ²⁹Tel Aviv University, Tel Aviv, Israel. ³⁰University of Virginia, Charlottesville, VA, USA. ³¹Kent State University, Kent, OH, USA. ³²University of Massachusetts, Amherst, MA, USA. ³³Facultad de Física, Universidad de Valencia, Valencia, Spain. ³⁴University of Ljubljana, Ljubljana, Slovenia. ³⁵Los Alamos National Laboratory, Los Alamos, NM, USA. ³⁶Norfolk State University, Norfolk, VA, USA. ³⁷Argonne National Laboratory, Lemont, IL, USA. ³⁸Kasetsart University, Chatuchak, Bangkok, Thailand. ³⁹Yerevan Physics Institute, Yerevan, Armenia. ⁴⁰George Washington University, Washington, DC, USA. ⁴¹INFN/Sezione di Roma, Roma, Italy. ⁴²Deceased: C. W. de Jager, S. Frullani, A. Saha, P. Solvignon. *e-mail: benali@jlab.org

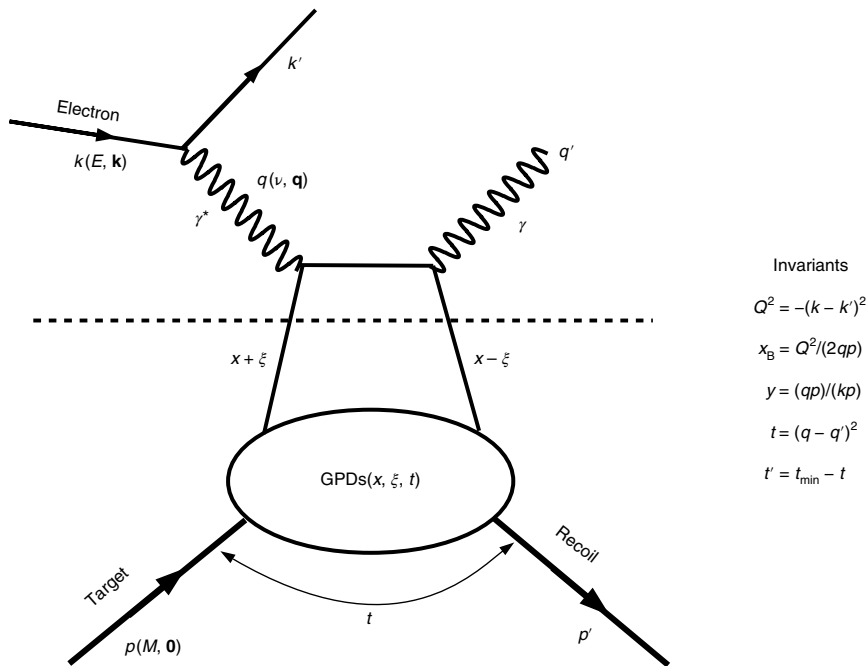


Fig. 1 | The handbag diagram for DVCS. In the kinematics of the experiment reported here $x_B=0.36$ for DVCS on the nucleon ($M=M_N$) and $x_B=0.18$ for DVCS on the coherent deuteron ($M=M_d$). The minimal $|t|$ value is $t_{\min}=Q^2[2(1-x_B)(1-\sqrt{1+\epsilon^2})+\epsilon^2]/(4x_B(1-x_B)+\epsilon^2)$, where $\epsilon^2=4x_B^2M^2/Q^2$.

allows a multidimensional description of the nucleon. In particular, GPDs correlate the transverse spatial structure of partons and their intrinsic longitudinal motion⁵, offering the possibility to access the quark (and gluon) orbital angular momentum⁶ and to elucidate the nucleon spin puzzle⁷. The nucleon structure is described by eight GPDs for each quark flavour q at leading twist. The leading twist describes the scattering off a single parton of the nucleon with no other partons participating in the process. Four of the leading-twist GPDs conserve the helicity of the parton (chiral-even GPDs), denoted by H^q , E^q , \tilde{H}^q and \tilde{E}^q , and the other four flip the parton helicity (chiral-odd GPDs), H_T^q , E_T^q , \tilde{H}_T^q and \tilde{E}_T^q (refs. ^{8,9}). Each GPD depends on three variables, x , ξ and t , where $x+\xi$ ($x-\xi$) is the longitudinal momentum fraction of the struck quark before (after) the scattering resulting in a squared four-momentum transfer t to the nucleon.

GPDs are involved in many hard exclusive processes such as deeply virtual Compton scattering (DVCS) and deeply virtual meson production, where a real photon and a meson are emitted respectively by the nucleon when probed with a virtual photon. In the Bjorken limit, when the virtuality Q^2 and the energy v of the virtual photon become very large at fixed x_B (see Fig. 1), QCD factorization theorems^{10,11} demonstrate that the DVCS amplitude can be factorized into a hard perturbative kernel and a soft part described by chiral-even GPDs, leading to the so-called handbag diagram of Fig. 1. Recent experimental studies on DVCS show that the Bjorken limit may already be reached at Q^2 values as low as 1.5 GeV² (refs. ^{12,13}). Experimentally, DVCS is indistinguishable from the Bethe–Heitler (BH) process, where the real photon is emitted by the incoming or the scattered electron.

The differential cross-section of photon electroproduction can then be written as¹⁴

$$\frac{d^4\sigma}{dQ^2 dx_B dt d\phi} = \frac{\alpha_{\text{QED}}^3 x_B \gamma^2}{8\pi Q^4 e^6 \sqrt{1+\epsilon^2}} [|\mathcal{T}_{\text{BH}}|^2 + |\mathcal{T}_{\text{DVCS}}|^2 + \mathcal{I}] \quad (1)$$

where ϕ is the azimuthal angle between the leptonic and hadronic planes¹⁵. The BH amplitude \mathcal{T}_{BH} is fully calculable in quantum electrodynamics with the nucleon FFs with 1% uncertainty. The interference and $|\mathcal{T}_{\text{DVCS}}|^2$ terms in equation (1) contain a finite $\cos(n\phi)$ series for \mathcal{I} ($n=0, \dots, 3$) and for $|\mathcal{T}_{\text{DVCS}}|^2$ ($n=0, \dots, 2$) (ref. ¹⁶). The different ϕ and beam-energy dependences of \mathcal{I} and $|\mathcal{T}_{\text{DVCS}}|^2$ at fixed x_B , Q^2 and t allow us to deduce the individual contributions of these terms¹⁷. Their Fourier harmonics can be expressed respectively as a function of linear and bilinear combinations of GPD convolutions with the perturbative kernel, called Compton form factors (CFFs)¹⁸. Photon electroproduction measurements at sufficiently high Q^2 are sensitive to different CFF combinations depending on the lepton and target polarization states^{12,13,17,19–38}. While the incident-beam helicity-dependent cross-section can access the imaginary part of the interference, which is sensitive to GPDs at $x=\pm\xi$, the helicity-independent cross-section measurements offer a stronger constraint since the real part of the interference probes GPD integrals over their full x -domain. For instance, the combination of leading-twist CFFs $\mathcal{F} \in \{\mathcal{H}, \mathcal{E}, \tilde{\mathcal{H}}\}$ appearing in the interference term for an unpolarized target reads^{18,39}

$$\text{Re}(C^{\mathcal{I}}) = \text{Re}\left(F_1 \mathcal{H} - \frac{t}{4M^2} F_2 \mathcal{E} + \xi(F_1 + F_2) \tilde{\mathcal{H}}\right) \quad (2)$$

where $F_1(t)$ ($F_2(t)$) is the Dirac (Pauli) FF, $\xi \approx \frac{x_B}{2-x_B}$ is the skewness variable in the Bjorken limit and

$$\text{Re}(\mathcal{F}) = \mathcal{P} \int_{-1}^1 dx \left[\frac{1}{x-\xi} \pm \frac{1}{x+\xi} \right] F(x, \xi, t) \quad (3)$$

Neutron GPDs are highly complementary to the proton ones. Their knowledge represents a mandatory step towards a better description of the partonic structure of the nucleon, even if their experimental measurement is more challenging to achieve. On the

one hand, the neutron appears to be the simplest way to perform a flavour decomposition of the u and d quark GPDs. Indeed, the quark flavour structure of a given GPD F , neglecting strange quarks, is written for a proton (p) and a neutron (n)

$$F^{p,n} = \frac{4}{9} F^{u,d} + \frac{1}{9} F^{d,u} \quad (4)$$

Contributions from strange quark GPDs are expected to be negligible on the basis of the size of strange flavour PDFs and the strange vector and axial-vector strange FFs of the nucleon, all of them very small compared with those of their u and d counterparts^{40,41}. On the other hand, the different FF values for a neutron and a proton allow a sensitivity to specific CFFs. For instance, equation (2), which is dominated by \mathcal{H} and $\tilde{\mathcal{H}}$ for the proton, becomes mainly sensitive to \mathcal{E} for the neutron due to the small value of F_1 and to the cancellation between u and d polarized parton distributions in $\tilde{\mathcal{H}}$ (ref. ⁴²). Measurements of the unpolarized $en \rightarrow eny$ (n-DVCS) cross-sections at low t become then of direct relevance in the determination of the quark angular momentum via Ji's sum rule⁶:

$$J^q = \frac{1}{2} \int_{-1}^1 x dx [H^q(x, \xi, t=0) + E^q(x, \xi, t=0)] \forall \xi, \quad (5)$$

since the x dependence of E^q is basically unknown, in contrast to H^q . The only existing n-DVCS data at large x_B are from the pioneering Jefferson Lab Hall A experiment E03-106 (ref. ²⁶), where the beam-helicity-dependent cross-section was determined at $x_B=0.36$, $Q^2=1.9 \text{ GeV}^2$ and $E=5.75 \text{ GeV}$. In this paper, we present $en \rightarrow eny$ unpolarized cross-section measurements at very close kinematics ($x_B=0.36$ and $Q^2=1.75 \text{ GeV}^2$) for two beam energies, $E=4.45$ and 5.55 GeV .

The data of the E08-025 experiment reported herein were acquired in Jefferson Lab Hall A. The extraction of the $n(e, e\gamma)n$ cross-section in the quasifree approximation is based on a controlled subtraction of data taken on liquid hydrogen (LH2) and liquid deuterium (LD2) targets, similarly to what was done in ref. ²⁶ and more recently in ref. ⁴³. The quasifree $p(e, e\gamma)p$ contribution is determined from the data of the E07-007 experiment¹⁷, the LH2 and LD2 targets being switched daily to minimize systematic errors. Scattered electrons were detected in the left-hand High Resolution Spectrometer⁴⁴ of Hall A, defining accurately the leptonic variables and the interaction vertex. Photons of more than 500 MeV were detected in an electromagnetic calorimeter consisting of a 13×16 array of $3 \times 3 \times 18.6 \text{ cm}^3$ PbF₂ crystals, placed at 1.1 m from the target and centred around the virtual photon direction. This configuration leads to a 2π coverage in ϕ and t ranging from -0.15 to -0.45 GeV^2 ($t'=t_{\min} - t \in [0, 0.3] \text{ GeV}^2$).

Figure 2 (top) shows the missing-mass-squared $M_X^2 = (q+p-q')^2$ spectrum of $D(e, e'\gamma)X$, where the target is assumed to be a nucleon at rest ($p=(M_N, \mathbf{0})$). Exclusive photon-electroproduction events are located around M_N^2 and are contaminated by three kinds of event: accidentals, photons from π^0 decays and semi-inclusive (SIDIS), equivalently associated DVCS¹⁵, events $eN \rightarrow e\gamma X$. The accidentals are determined by analysing events that are outside the coincidence window. Their relative contribution is reduced by applying the selection criterion $M_X^2 > 0.5 \text{ GeV}^2$ to the data set. The number of π^0 decays yielding only one photon in the calorimeter acceptance is estimated by generating thousands of decays for each detected π^0 (ref. ¹²). The subtracted number of events $N_{\pi^0}^i$ in a bin i is

$$N_{\pi^0}^i = \sum_{j=1}^{N_{\pi^0}} \frac{N_{\pi^0}^{j,i}}{N_2^j} \pm \sqrt{\sum_{j=1}^{N_{\pi^0}} \left(\frac{N_{\pi^0}^{j,i}}{N_2^j} \right)^2} \quad (6)$$

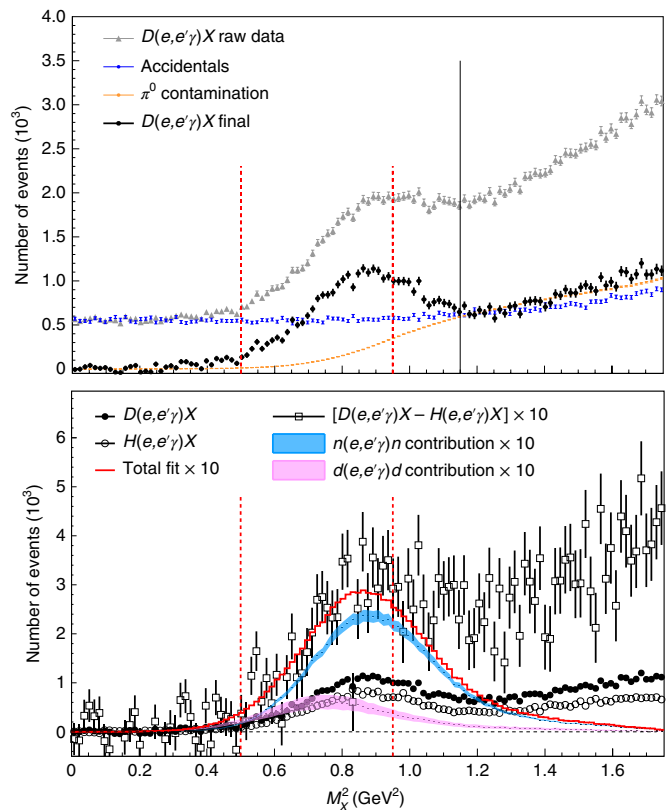


Fig. 2 | Missing-mass-squared distributions. Top: the grey triangles show the raw data distribution of $D(e, e'\gamma)X$ for $E=4.45 \text{ GeV}$ and the bin $\langle t \rangle = -0.32 \text{ GeV}^2$, integrated over ϕ . Subtraction of the contributions of accidentals and π^0 contamination from the raw spectrum yields the histogram in black circles (also shown in the bottom plot). The error bars of the raw data and the accidentals contribution correspond to 1 s.d. and are calculated as the square root of the number of detected events. The error bars of the π^0 contamination contribution are calculated following equation (6). The pion production threshold is represented by the solid vertical line at 1.15 GeV^2 . The range in $M_X^2 \in [0.5, 0.95] \text{ GeV}^2$ used in the analysis is shown by the dashed vertical lines. Bottom: the difference between the $D(e, e'\gamma)X$ (black circles) and normalized Fermi-smeared $H(e, e'\gamma)X$ events (white circles), after accidental and π^0 subtraction, is shown by the histogram in white squares (scaled by a factor of 10 for clarity). The blue and magenta bands (both scaled by a factor of 10) show the simulated $n(e, e'\gamma)n$ and $d(e, e'\gamma)d$ yields, respectively, fitted to the data by minimizing equation (8). These bands include the s.d. statistical uncertainty of the fit. The total fit to the distribution of white squares is shown by the red histogram.

where the sum runs over the total number N_{π^0} of detected π^0 events. For each of these j events, $N_{\pi^0}^{j,i}$ is the number of simulated decays yielding one photon in bin i and fulfilling the DVCS selection criteria, whereas N_2^j is the number of decays that yield two photons within the experimental acceptance. The SIDIS events are essentially located above the pion production threshold ($(M_N + M_\pi)^2 \approx 1.15 \text{ GeV}^2$). However, the nominal selection criterion $M_X^2 < 0.95 \text{ GeV}^2$ is applied to minimize any possible contamination to the exclusive yield due to resolution effects. A bin-dependent systematic error is attributed later to the results by studying the stability of the extracted cross-sections when varying this nominal selection criterion. After the subtraction of accidentals and the π^0 background, the remaining events in the exclusive

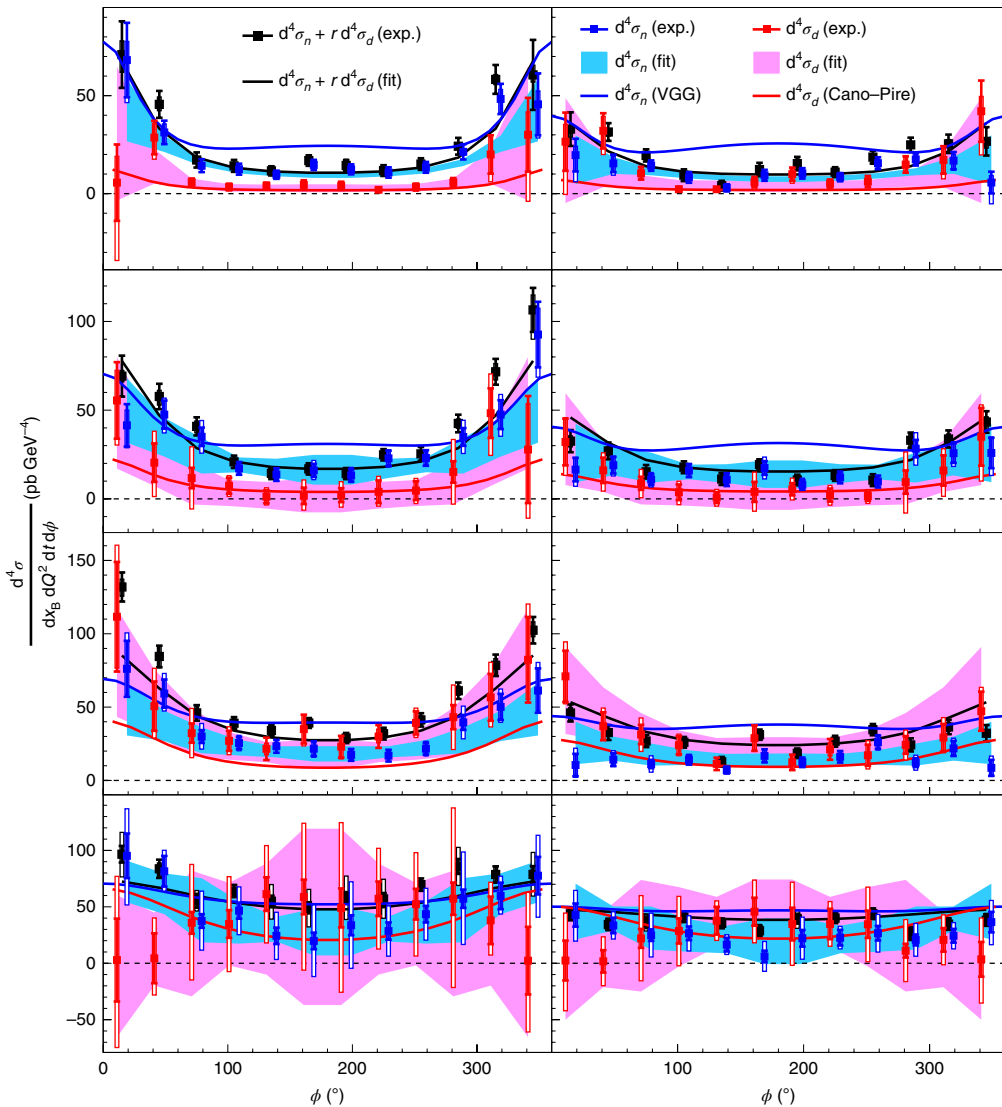


Fig. 3 | Beam-helicity-independent cross-sections. The black points show the sum of the neutron and coherent deuteron cross-sections $d^4\sigma_n + r d^4\sigma_d$, where $r = (dx_B^d dt^d)/(dx_B^n dt^n) \approx \frac{M_N}{M_d} \approx 0.5$ is the ratio of the deuteron and neutron acceptances. The error bars show the s.d. statistical uncertainty and the boxes around the points show the total s.d. systematic uncertainty. The blue (red) points show the neutron (coherent deuteron) contribution $d^4\sigma_n$ ($d^4\sigma_d$) with its s.d. statistical (bars) and systematic (boxes) uncertainties. The blue and magenta bands show the fit to $d^4\sigma_n$ and $d^4\sigma_d$ respectively with the s.d. systematic and statistical errors of the fit added quadratically. The results correspond to $x_B = 0.36$ for the neutron and $x_B = 0.18$ for the coherent deuteron at $E = 4.45$ GeV (left) and $E = 5.55$ GeV (right). From top to bottom, the squared momentum transfer corresponds to $-\langle t \rangle = 0.40, 0.32, 0.25$ and 0.18 GeV 2 for the neutron and $-\langle t \rangle = 0.33, 0.26, 0.20$ and 0.15 GeV 2 for the deuteron. The solid blue (red) lines are theoretical calculations for the neutron (coherent deuteron) from refs. 49,50 (ref. 48).

region can be decomposed, within the impulse approximation, into coherent elastic events $d(e, e'\gamma)d$ and two incoherent quasielastic channels

$$D(e, e'\gamma)X = d(e, e'\gamma)d + n(e, e'\gamma)n + p(e, e'\gamma)p \quad (7)$$

where $X = np \oplus d$. The extraction of the $ed \rightarrow ed\gamma$ cross-section is also considered in this work. Its expression is similar to equation (1) and depends on deuteron CFFs involving, at leading twist, nine spin-1 target GPDs⁴⁶. The quasifree $p(e, e'\gamma)X$ contribution is determined by normalizing the LH2 data to the luminosity of the LD2 data and by adding statistically the Fermi momentum⁴⁷ of bound protons inside the deuteron. The width variation of the M_X^2 distribution due to the Fermi-momentum smearing is less than 1% and thus its uncertainty is negligible in the final results.

Figure 2 (bottom) shows the result of the subtraction of the background-free LH2 from the LD2 data. The resulting events passing the M_X^2 exclusivity selection criterion correspond to the $d(e, e'\gamma)d$ and $n(e, e'\gamma)n$ channels, which are kinematically separated by $\Delta M_X^2 = t(1 - M_N/M_d) \approx t/2$. The exclusive data are divided into $12 \times 2 \times 5 \times 30$ bins in ϕ , E , t and M_X^2 respectively. The results will be presented as a function of ϕ , E and t , the binning on M_X^2 serving only to separate the $d(e, e'\gamma)d$ and $n(e, e'\gamma)n$ contributions by exploiting their kinematic shift.

The extraction of the cross-sections is based on a simultaneous fit of all experimental bins by means of a Monte Carlo simulation of $d(e, e'\gamma)d$ and $n(e, e'\gamma)n$ reactions. After applying the exclusivity M_X^2 selection criterion, the remaining number of simulated events N_i^{sim} in bin i is adjusted to the corresponding number of experimental events N_i^{exp} by minimizing

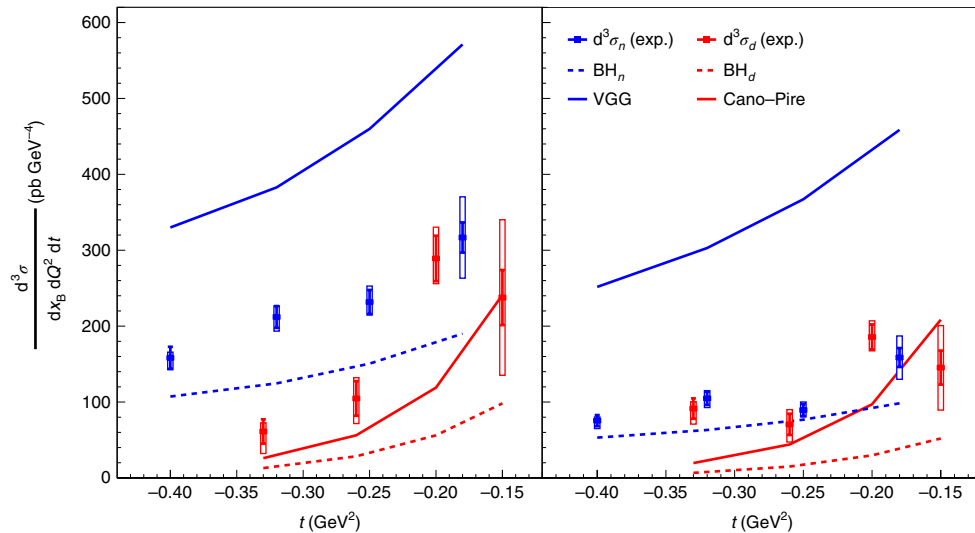


Fig. 4 | Neutron and deuteron cross-sections integrated over ϕ . The blue (red) points correspond to the $en \rightarrow en\gamma$ ($ed \rightarrow ed\gamma$) experimental cross-sections $d^3\sigma_{n(d)}/dQ^2 dx_B dt$ for beam energy $E=4.45$ GeV (left) and $E=5.55$ GeV (right). The error bars show the s.d. statistical uncertainty and the boxes around the points show the total s.d. systematic uncertainty. Respective BH contributions are shown by the dashed lines, whereas the Vanderhaeghen–Guichon–Guidal model^{49,50} for the neutron and Cano–Pire model⁴⁸ for the deuteron are represented by the solid curves.

$$\chi^2 = \sum_{i=1}^{3,600} \left(\frac{N_i^{\text{exp}} - N_i^{\text{sim}}}{\delta_i^{\text{exp}}} \right)^2 \quad (8)$$

where δ_i^{exp} is the statistical uncertainty of N_i^{exp} . The free parameters of the fit are a set of neutron and deuteron CFF combinations for each t bin. Figure 3 presents the ϕ -dependent cross-sections for both beam energies and for all t bins excepting the highest- $|t|$ one, which was only used to account for bin migration effects. The uncertainties on the extracted neutron and coherent deuteron cross-sections take into account the ΔM_X^2 correlation between these two contributions, which varies between -0.96 at low $|t|$ and -0.79 at high $|t|$. Point-to-point systematic uncertainties due to calorimeter calibration, simulation smearing and the missing-mass selection criterion are added in quadrature to a 3.1% normalization uncertainty (Methods) and are represented by the boxes around the data points in Fig. 3. Note that the normalization uncertainties (3.1%) are much smaller than the point-to-point uncertainties (which average to 37%), and their effect is negligible.

When integrated over ϕ , the neutron results exhibit a significant deviation from the BH contribution, especially for $E=4.45$ GeV, as shown in Fig. 4. At $E=4.45$ GeV the coherent deuteron cross-sections are smaller than the neutron cross-sections for the two highest- $|t|$ bins, as could be expected from Fig. 2 and by the rapid relative decrease of the deuteron FFs at large $|t|$. The coherent deuteron results are relatively well described, within uncertainties, by theoretical calculations based on deuteron GPDs⁴⁸, whereas the Vanderhaeghen–Guichon–Guidal model^{49,50} significantly overshoots results for the neutron. This model reproduces proton DVCS data much better (see ref. ¹³ for example), so the disagreement for the neutron is perhaps symptomatic of the paucity of experimental constraints on the GPD E .

The simultaneous fit of both beam energy settings allows us to independently extract the contribution from the $|\mathcal{T}_{\text{DVCS}}|^2$ and BH-DVCS interference terms. These are shown in Fig. 5 for the neutron. The analysis has been performed within the recent formalism by Braun et al.³⁹, which accounts for kinematical power corrections of $\mathcal{O}(t/Q^2)$ and $\mathcal{O}(M^2/Q^2)$. Previous results on the proton¹⁷ showed the necessity to include higher-twist (HT) or next-to-leading-order

(NLO) CFFs in the analysis to accurately reproduce the azimuthal angular dependence of the cross-section. Fits have been performed within two scenarios that yield equally good results. An HT scenario includes, in addition to the helicity-conserving CFFs \mathcal{H}_{++} , $\bar{\mathcal{H}}_{++}$ and \mathcal{E}_{++} , the HT CFFs \mathcal{H}_{0+} , $\bar{\mathcal{H}}_{0+}$ and \mathcal{E}_{0+} . The NLO scenario includes helicity-conserving CFFs and the NLO CFFs \mathcal{H}_{+-} , $\bar{\mathcal{H}}_{+-}$ and \mathcal{E}_{+-} (ref. ³⁹). The absence of $\tilde{\mathcal{E}}$ from the interference term makes it difficult to separate its real and imaginary parts and it was not included in the fit. The separation of the $|\mathcal{T}_{\text{DVCS}}|^2$ and interference terms in Fig. 5 shows slight variations depending on which scenario is considered, but with a significant signal from $|\mathcal{T}_{\text{DVCS}}|^2$ for all values of ϕ and t .

The notable size of the $|\mathcal{T}_{\text{DVCS}}|^2$ and interference terms constitutes observation of DVCS off a quasifree-neutron target and allows us, when combined with results off the proton, to probe nucleon GPDs at the level of quark flavours u and d by exploiting equation (4). A fit of all the available proton^{12,17} and neutron²⁶ cross-sections from Hall A at $Q^2=1.5\text{--}2.3$ GeV 2 and $x_B=0.36$, including the present results, is performed within the Braun–Manashov–Müller–Pirnay parametrization³⁹ of the DVCS amplitude. Fits were performed in the same two scenarios as described above, HT and NLO, but for each flavour of quarks, u and d . The fit quality is quite reasonable across the whole data set (Extended Data Figs. 1 and 2), with χ^2/ndf (number of degrees of freedom) ranging from 399/444 (407/444) to 533/470 (529/470) for the HT (NLO) scenario. Figure 6 shows the results for the real and imaginary parts of \mathcal{H}_{++} , $\bar{\mathcal{H}}_{++}$ and \mathcal{E}_{++} . The better accuracy of the proton experimental cross-sections is reflected in the u CFF results. Notice that the uncertainties in Fig. 6 are dominated by correlations in the fit parameters rather than by the accuracy of the experimental cross-section values.

The experimental results in Fig. 6 are compared with theoretical predictions based on a reggeized diquark model of GPDs^{51,52}. The flavours u and d for CFF \mathcal{H}_{++} show the same sign, for both the real and imaginary parts, in the model. Data are also consistent, within uncertainties, with the same sign of u and d for \mathcal{H}_{++} . This is in agreement with what is observed in the forward limit⁴⁰ and the predictions of SU(N_c) gauge theory with a large number N_c of colours⁴². In both the forward and the large- N_c limits GPD \tilde{H} has opposite signs for flavours u and d , which seems also to be the case for the

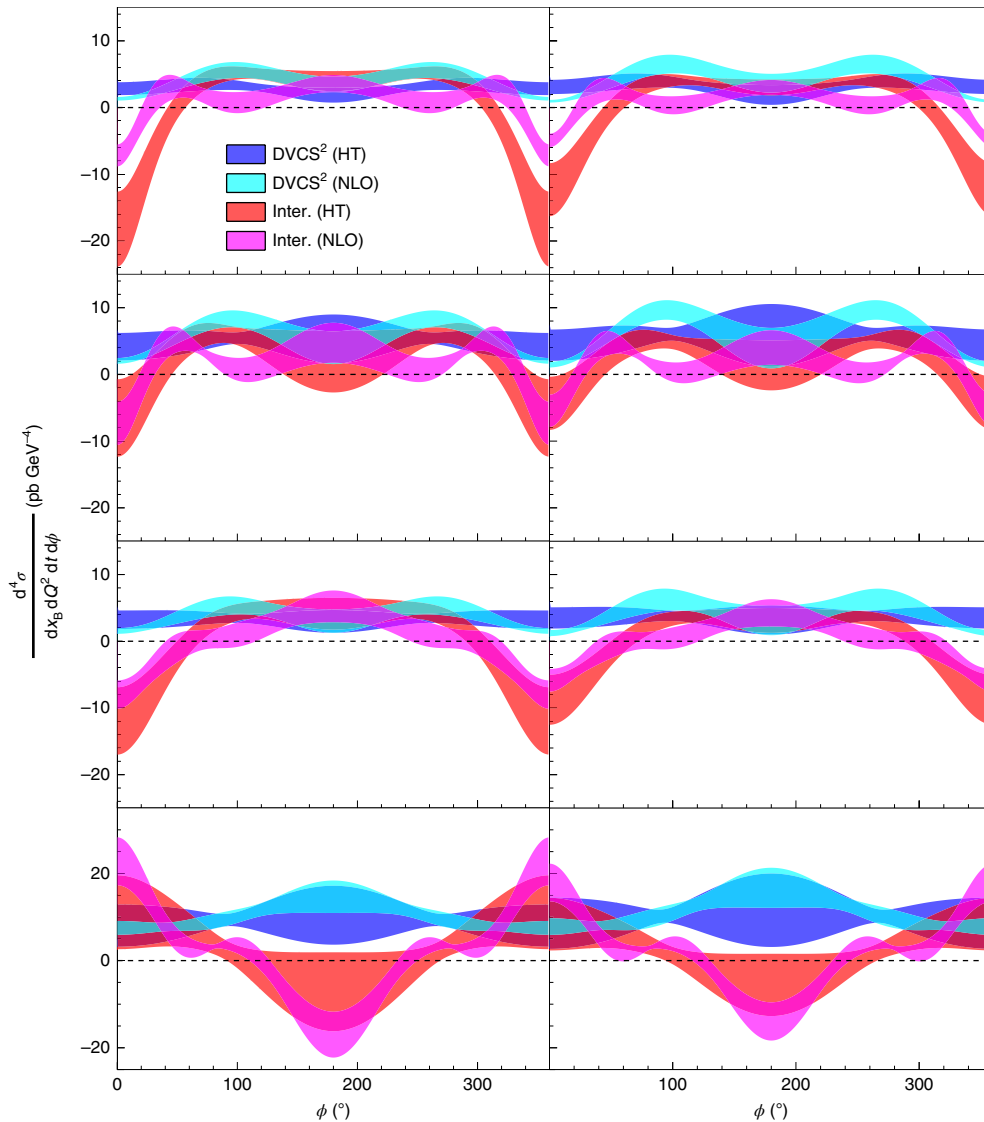


Fig. 5 | Separation of the $|T_{\text{DVCS}}^n|^2$ and I^n terms. The dark-blue and light-blue bands show the contribution to the $e n \rightarrow e n y$ cross-section of the $|T_{\text{DVCS}}^n|^2$ term in the HT and NLO scenarios respectively. The red (magenta) band shows the contribution of the I^n term in the HT (NLO) scenario. The widths of the bands correspond to the s.d. statistical uncertainty of the fits. The results are for $E=4.45 \text{ GeV}$ (left) and $E=5.55 \text{ GeV}$ (right). From the top to the bottom, the squared momentum transfer corresponds to $-\langle t \rangle = 0.40, 0.32, 0.25$ and 0.18 GeV^2 . The fits are performed within the cross-section formalism of ref.³⁹

data. Notice that there is a change of sign between the imaginary and the real parts of $\tilde{\mathcal{H}}$. While in this case this effect is well reproduced by the model, it highlights the non-trivial functional form of the GPDs, which can flip the sign of the integral defining the real part of the CFFs (equation (3)). The CFF \mathcal{E}_{++} shows interesting features. Its imaginary parts suggest opposite signs for flavours u and d . This matches the signs of the u and d anomalous magnetic moments $\kappa_{u,d}^{ud}$, which give the normalization of the first moment of E , and also agrees with the large- N_c limit⁴². However, the values for quark u are not well reproduced by the theoretical model. This is also the case, to some extent, for $\text{Im}(\mathcal{H}_{++})$, $\text{Re}(\tilde{\mathcal{H}}_{++})$ and $\text{Im}(\tilde{\mathcal{H}}_{++})$. The Ji sum rule (equation (5)) results of the model in ref.⁵¹ are presented in ref.⁵³ (Fig. 19 and Table V). This model is flexible, and since there are few constraints on CFF \mathcal{E}_{++} it is likely that a revision of the model parameters would improve the description of these data, and result in a shift in the estimated values of $J_{u,d}$ —the contribution of up and down quarks to the spin of the proton.

The forward limit of GPD E is not measurable from any known inclusive process, and very few observables (such as DVCS off the neutron, and DVCS on a transversely polarized target) have high sensitivity to it. While the uncertainties in the flavour separation presented here are still large, the data clearly show the potential and the sensitivity to this very challenging yet fundamental quantity. The upcoming and in-process experiments on proton and neutron DVCS with Jefferson Lab at 12 GeV will soon allow us to better pin down the GPD E and its flavour decomposition.

Online content

Any methods, additional references, Nature Research reporting summaries, source data, extended data, supplementary information, acknowledgements, peer review information; details of author contributions and competing interests; and statements of data and code availability are available at <https://doi.org/10.1038/s41567-019-0774-3>.

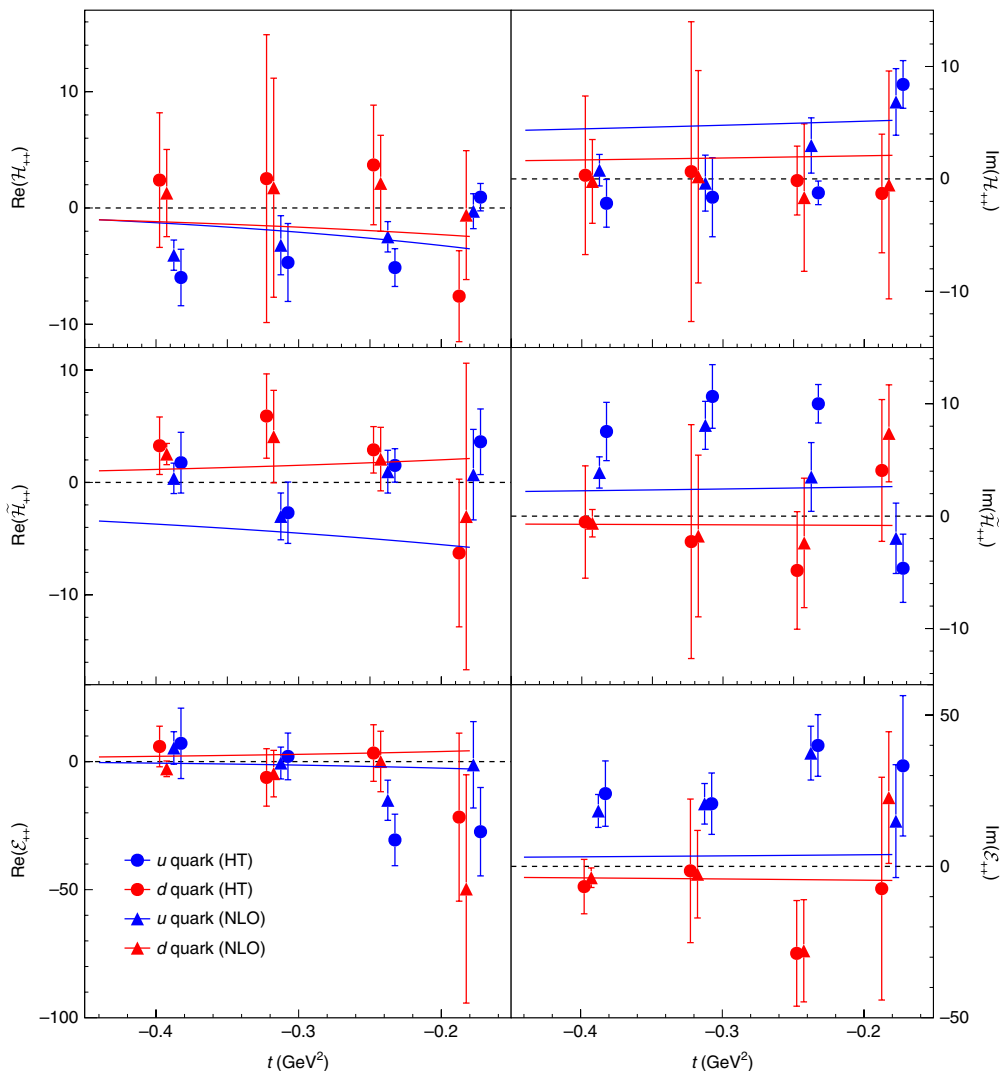


Fig. 6 | Flavour separation of helicity-conserved CFFs. The points represent the real and imaginary parts of u and d helicity-conserved CFFs \mathcal{H}_{++} , $\tilde{\mathcal{H}}_{++}$ and \mathcal{E}_{++} in both the HT and NLO scenarios. The error bars correspond to 1 s.d. and take into account the statistical and the systematic uncertainties of the fitted cross-sections. Solid lines present the predictions of a reggeized diquark model of GPDs^{51,52}.

Received: 3 November 2018; Accepted: 1 November 2019;
Published online: 27 January 2020

References

- Hofstadter, R. & McAllister, R. W. Electron scattering from the proton. *Phys. Rev.* **98**, 217–218 (1955).
- Taylor, R. E. Deep inelastic scattering: the early years. *Rev. Mod. Phys.* **63**, 573–595 (1991).
- Radyushkin, A. V. Nonforward parton distributions. *Phys. Rev. D* **56**, 5524–5557 (1997).
- Müller, D., Robaschik, D., Geyer, B., Dittes, F. M. & Horejsi, J. Wave functions, evolution equations and evolution kernels from light-ray operators of QCD. *Fortschr. Phys.* **42**, 101–141 (1994).
- Burkardt, M. Impact parameter space interpretation for generalized parton distributions. *Int. J. Mod. Phys. A* **18**, 173–207 (2003).
- Ji, X. Gauge invariant decomposition of nucleon spin. *Phys. Rev. Lett.* **78**, 610–613 (1997).
- Aidala, C. A., Bass, S. D., Hasch, D. & Mallot, G. K. The spin structure of the nucleon. *Rev. Mod. Phys.* **85**, 655–691 (2013).
- Hoodbhoy, P. & Ji, X. Helicity-flip off-forward parton distributions of the nucleon. *Phys. Rev. D* **58**, 054006 (1998).
- Diehl, M. Generalized parton distributions. *Phys. Rep.* **388**, 41–277 (2003).
- Collins, J. C., Frankfurt, L. & Strikman, M. Factorization for hard exclusive electroproduction of mesons in QCD. *Phys. Rev. D* **56**, 2982–3006 (1997).
- Ji, X. & Osborne, J. One-loop corrections and all order factorization in deeply virtual Compton scattering. *Phys. Rev. D* **58**, 094018 (1998).
- Defurne, M. et al. E00-110 experiment at Jefferson Lab Hall A: deeply virtual Compton scattering off the proton at 6 GeV. *Phys. Rev. C* **92**, 055202 (2015).
- Jo, H. S. et al. Cross sections for the exclusive photon electroproduction on the proton and generalized parton distributions. *Phys. Rev. Lett.* **115**, 212003 (2015).
- Belitsky, A. & Müller, D. Exclusive electroproduction revisited: treating kinematical effects. *Phys. Rev. D* **82**, 074010 (2010).
- Bacchetta, A., D'Alesio, U., Diehl, M. & Müller, C. A. Single-spin asymmetries: the Trento conventions. *Phys. Rev. D* **70**, 117504 (2004).
- Diehl, M., Gousset, T., Pire, B. & Ralston, J. P. Testing the handbag contribution to exclusive virtual Compton scattering. *Phys. Lett. B* **411**, 193–202 (1997).
- Defurne, M. et al. A glimpse of gluons through deeply virtual Compton scattering on the proton. *Nat. Commun.* **8**, 1408 (2017).
- Belitsky, A., Müller, D. & Ji, Y. Compton scattering: from deeply virtual to quasi-real. *Nucl. Phys. B* **878**, 214–268 (2014).
- Airapetian, A. et al. Measurement of the beam spin azimuthal asymmetry associated with deeply-virtual Compton scattering. *Phys. Rev. Lett.* **87**, 182001 (2001).
- Stepanyan, S. et al. Observation of exclusive deeply virtual Compton scattering in polarized electron beam asymmetry measurements. *Phys. Rev. Lett.* **87**, 182002 (2001).
- Adloff, C. et al. Measurement of deeply virtual Compton scattering at HERA. *Phys. Lett. B* **517**, 47–58 (2001).

22. Chekanov, S. et al. Measurement of deeply virtual Compton scattering at HERA. *Phys. Lett. B* **573**, 46–62 (2003).
23. Aktas, A. et al. Measurement of deeply virtual Compton scattering at HERA. *Eur. Phys. J. C* **44**, 1–11 (2005).
24. Chen, S. et al. Measurement of deeply virtual Compton scattering with a polarized proton target. *Phys. Rev. Lett.* **97**, 072002 (2006).
25. Airapetian, A. et al. The beam-charge azimuthal asymmetry and deeply virtual Compton scattering. *Phys. Rev. D* **75**, 011103 (2007).
26. Mazouz, M. et al. Deeply virtual Compton scattering off the neutron. *Phys. Rev. Lett.* **99**, 242501 (2007).
27. Aaron, F. D. et al. Measurement of deeply virtual Compton scattering and its t -dependence at HERA. *Phys. Lett. B* **659**, 796–806 (2008).
28. Girod, F. et al. Measurement of deeply virtual Compton scattering beam-spin asymmetries. *Phys. Rev. Lett.* **100**, 162002 (2008).
29. Airapetian, A. et al. Measurement of azimuthal asymmetries with respect to both beam charge and transverse target polarization in exclusive electroproduction of real photons. *J. High Energy Phys.* **06**, 066 (2008).
30. Chekanov, S. et al. Measurement of the Q^2 , W and t dependences of deeply virtual Compton scattering at HERA. *J. High Energy Phys.* **05**, 108 (2009).
31. Gavalian, G. et al. Beam spin asymmetries in deeply virtual Compton scattering (DVCS) with CLAS at 4.8 GeV. *Phys. Rev. C* **80**, 035206 (2009).
32. Aaron, F. D. et al. Deeply virtual Compton scattering and its beam charge asymmetry in $e \pm p$ collisions at HERA. *Phys. Lett. B* **681**, 391–399 (2009).
33. Airapetian, A. et al. Separation of contributions from deeply virtual Compton scattering and its interference with the Bethe–Heitler process in measurements on a hydrogen target. *J. High Energy Phys.* **11**, 083 (2009).
34. Airapetian, A. et al. Exclusive leptoproduction of real photons on a longitudinally polarised hydrogen target. *J. High Energy Phys.* **06**, 019 (2010).
35. Airapetian, A. et al. Measurement of double-spin asymmetries associated with deeply virtual Compton scattering on a transversely polarized hydrogen target. *Phys. Lett. B* **704**, 15–23 (2011).
36. Airapetian, A. et al. Beam-helicity and beam-charge asymmetries associated with deeply virtual Compton scattering on the unpolarised proton. *J. High Energy Phys.* **07**, 032 (2012).
37. Airapetian, A. et al. Beam-helicity asymmetry arising from deeply virtual Compton scattering measured with kinematically complete event reconstruction. *J. High Energy Phys.* **10**, 042 (2012).
38. Hirlinger Saylor, N. et al. Measurement of unpolarized and polarized cross sections for deeply virtual Compton scattering on the proton at Jefferson Laboratory with CLAS. *Phys. Rev. C* **98**, 045203 (2018).
39. Braun, V. M., Manashov, A. N., Müller, D. & Pirnay, B. M. Deeply virtual Compton scattering to the twist-four accuracy: impact of finite- t and target mass corrections. *Phys. Rev. D* **89**, 074022 (2014).
40. Dulat, S. et al. New parton distribution functions from a global analysis of quantum chromodynamics. *Phys. Rev. D* **93**, 033006 (2016).
41. Maas, F. E. & Paschke, K. D. Strange nucleon form-factors. *Prog. Part. Nucl. Phys.* **95**, 209–244 (2017).
42. Goeke, K. et al. Hard exclusive reactions and the structure of hadrons. *Prog. Part. Nucl. Phys.* **47**, 401–515 (2001).
43. Mazouz, M. et al. Rosenbluth separation of the π^0 electroproduction cross section off the neutron. *Phys. Rev. Lett.* **118**, 222002 (2017).
44. Alcorn, J. et al. Basic instrumentation for Hall A at Jefferson Lab. *Nucl. Instrum. Methods A* **522**, 294–346 (2004).
45. Guichon, P. A. M., Mossé, L. & Vanderhaeghen, M. Pion production in deeply virtual Compton scattering. *Phys. Rev. D* **68**, 034018 (2003).
46. Kirchner, A. & Müller, D. Deeply virtual Compton scattering off nuclei. *Eur. Phys. J. C* **32**, 347–375 (2003).
47. Lacombe, M. et al. Parametrization of the Paris N-N potential. *Phys. Rev. C* **21**, 861–873 (1980).
48. Cano, F. & Pire, B. Deep electroproduction of photons and mesons on the deuteron. *Eur. Phys. J. A* **19**, 423–438 (2004).
49. Vanderhaeghen, M., Guichon, P. A. M. & Guidal, M. Hard electroproduction of photons and mesons on the nucleon. *Phys. Rev. Lett.* **80**, 5064–5067 (1998).
50. Vanderhaeghen, M., Guichon, P. A. M. & Guidal, M. Deeply virtual electroproduction of photons and mesons on the nucleon: leading order amplitudes and power corrections. *Phys. Rev. D* **60**, 094017 (1999).
51. Goldstein, G. R., Gonzalez Hernandez, J. O. & Liuti, S. Flexible parametrization of generalized parton distributions from deeply virtual Compton scattering observables. *Phys. Rev. D* **84**, 034007 (2011).
52. Goldstein, G. R., Gonzalez Hernandez, J. O. & Liuti, S. Flexible parametrization of generalized parton distributions: the chiral-odd sector. *Phys. Rev. D* **91**, 114013 (2015).
53. Gonzalez-Hernandez, J. O., Liuti, S., Goldstein, G. R. & Kathuria, K. Interpretation of the flavor dependence of nucleon form factors in a generalized parton distribution model. *Phys. Rev. C* **88**, 065206 (2013).

Publisher's note Springer Nature remains neutral with regard to jurisdictional claims in published maps and institutional affiliations.

© The Author(s), under exclusive licence to Springer Nature Limited 2020

Methods

A thorough bin-dependent monitoring of the experimental calibration and resolution between LH2 and LD2 data is performed to ensure a proper subtraction of the $p(e, e'\gamma)p$ contribution from the exclusive $D(e, e'\gamma)X$ yield. This monitoring is based on the reconstruction of the π^0 and the nucleon squared masses from respectively the two-photon invariant-mass $(q_1 + q_2)^2$ (where q_1 and q_2 are the four-momenta of each photon) and the missing-mass $(q + p - q_1 - q_2)^2$ distributions in π^0 electroproduction events⁵⁴. The energy calibration coefficients are adjusted to best reproduce the values of the π^0 and nucleon masses in each bin in t and ϕ . Similarly, the energy resolution of events in the LH2 data is adjusted for each of the bins to match the π^0 and nucleon mass resolutions observed in the LD2 data.

The simulation used in the cross-section extraction is based on the GEANT4 toolkit. It takes into account the detector acceptance, the calculated pure BH contributions from the neutron and deuteron, and the kinematic weights appearing in the cross-section harmonics of the BH-DVCS interference terms and $|\mathcal{T}_{\text{DVCS}}|^2$ terms. Following the prescriptions in ref.⁵⁵, the simulation also includes the emission of hard photons (within the range of the missing-mass-squared spectrum of Fig. 2), and we apply a correction factor to the extracted cross-sections, to account for virtual photon and soft-real photon emission. This correction factor was 0.94 for the specific neutron kinematics reported here. We assign a 2% systematic uncertainty to this factor, on the basis of variations of neutron versus proton, varying the neutron DVCS model in the radiative correction calculation, a very small ϕ dependence, and differing procedures for exponentiating the soft photons. The calorimeter energy resolution in the simulation is smeared to fit the experimental one by reproducing the exclusive M_x^2 distribution of $H(e, e'\gamma)X$ with $p(e, e'\gamma)p$ simulated events. The obtained bin-by-bin smearing factors are then applied to the $d(e, e'\gamma)d$ and the Fermi-smeared $n(e, e'\gamma)n$ simulated data. This allows a proper computation of the experimental acceptance by applying identical selection criteria to experimental and simulated data, and correcting the final results for bin migration effects. This procedure introduces a bin-dependent systematic uncertainty, which is added quadratically to a 3.1% normalization uncertainty. The 3.1% value originates from the uncertainties on the radiative corrections (2%), the electron acceptance (1%) and multitrack correction (0.5%), the photon multicluster correction (0.5%), the data acquisition deadtime and luminosity (2%).

Data availability

Data that support the findings of this study are publicly available at <https://userweb.jlab.org/~mazouz/NP/>.

Code availability

The computer codes that support the plots within this paper and the findings of this study are available from M. Mazouz on request.

References

- 54. Mazouz, M. Energy calibration of laterally segmented electromagnetic calorimeters based on neutral pion detection. *Nucl. Sci. Tech.* **28**, 155 (2017).
- 55. Vanderhaeghen, M. et al. QED radiative corrections to virtual Compton scattering. *Phys. Rev. C* **62**, 025501 (2000).

Acknowledgements

We acknowledge the essential work of the Jefferson Lab accelerator staff and the Hall A technical staff. This work was supported by the Department of Energy (DOE), the National Science Foundation, the French Centre National de la Recherche Scientifique, the Agence Nationale de la Recherche, the Commissariat à l'énergie atomique et aux énergies alternatives and P2IO Laboratory of Excellence. Jefferson Science Associates, LLC, operates Jefferson Lab for the US DOE under US DOE contract DE-AC05-06OR23177.

Author contributions

The Jefferson Lab Hall A Collaboration constructed and operated the experimental equipment used in this experiment. Data were taken by a large number of collaboration members. The authors who performed data analyses and Monte Carlo simulations were M. Benali, C.D., M. Mazouz and C.M.C. The main authors of this manuscript were M. Benali, M. Mazouz, C.M.C., C.H., J.R. and A.C. It was reviewed by the entire collaboration before publication, and all authors approved the final version of the manuscript.

Competing interests

The authors declare no competing interests.

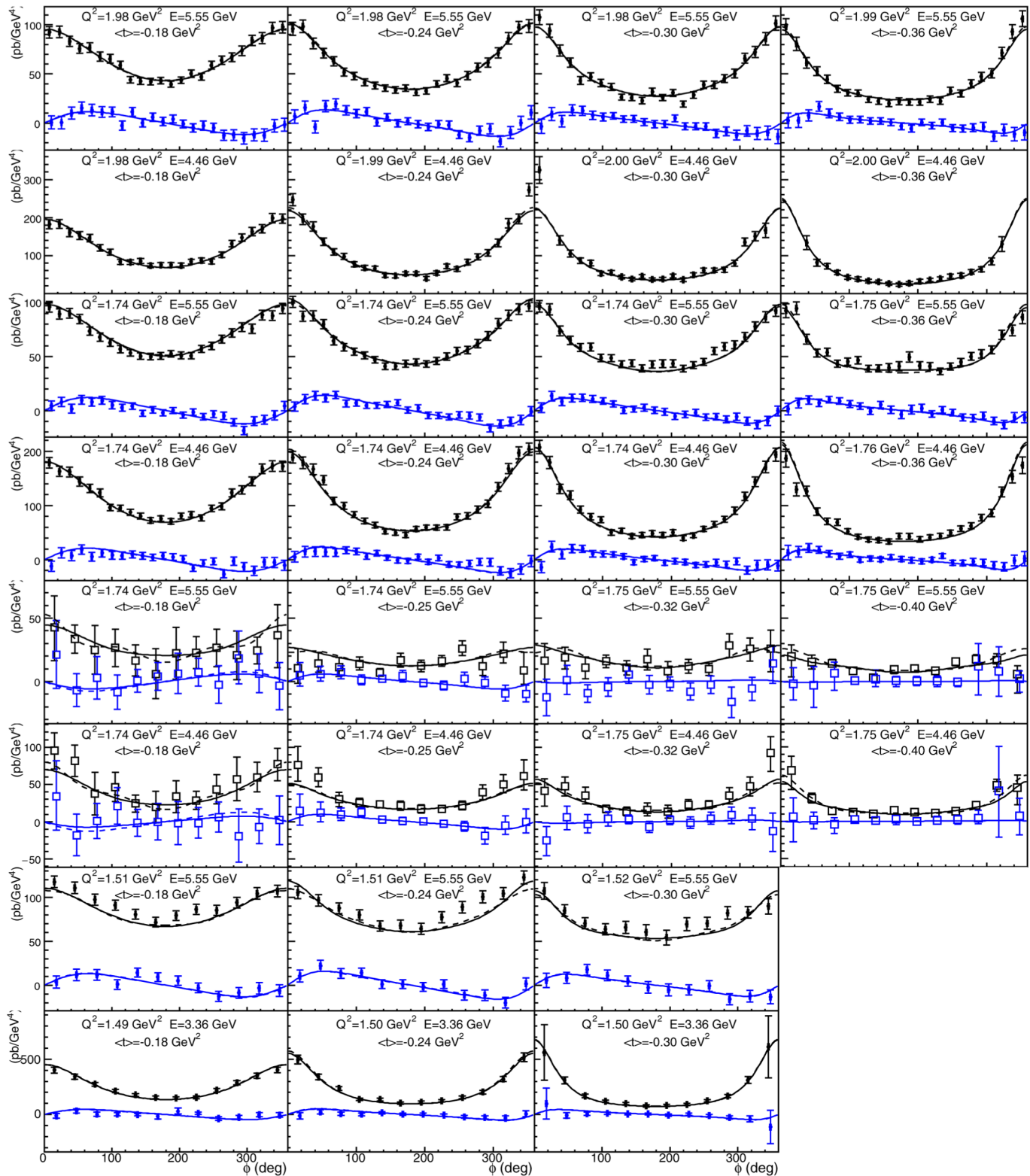
Additional information

Extended data is available for this paper at <https://doi.org/10.1038/s41567-019-0774-3>.

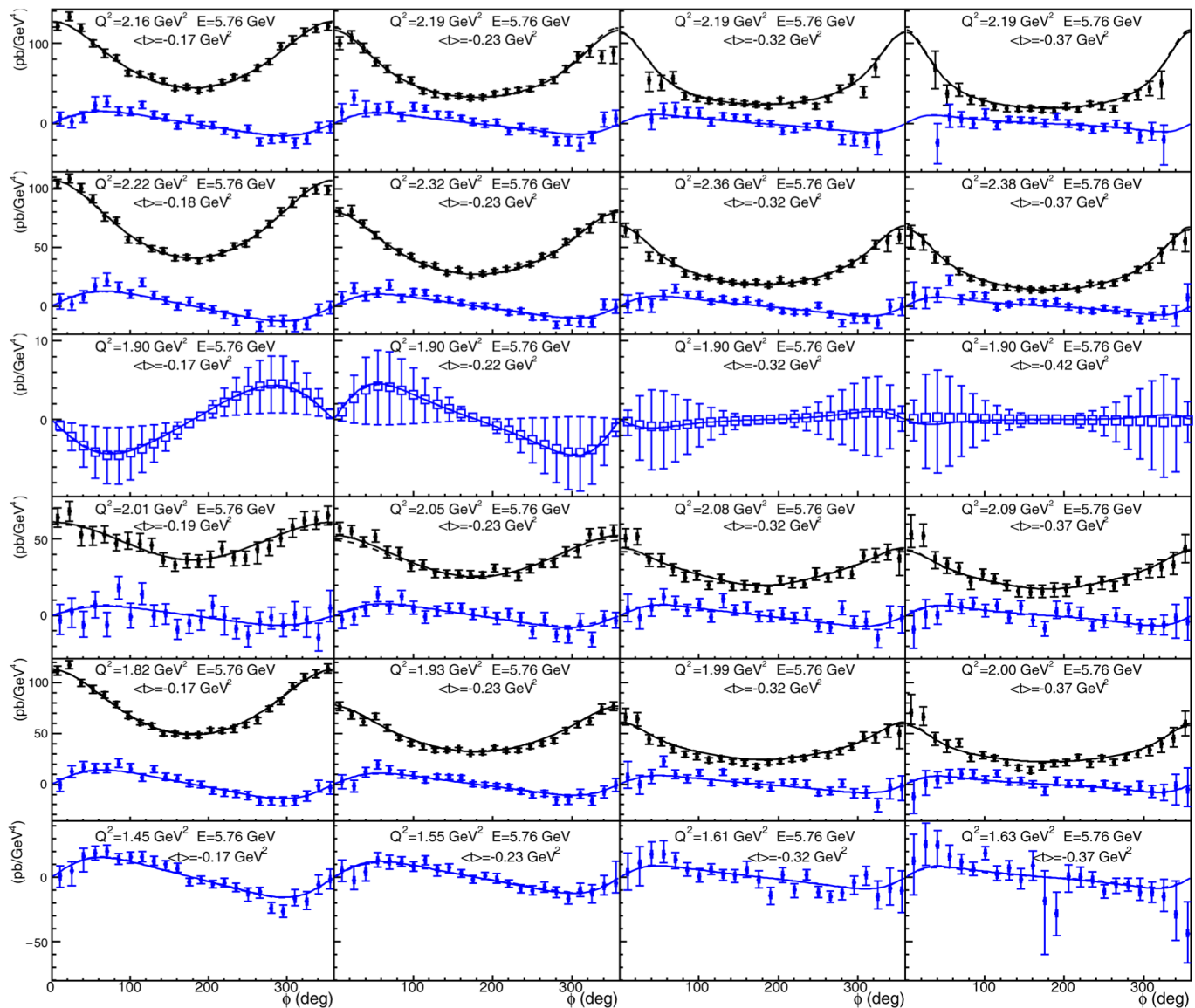
Supplementary information is available for this paper at <https://doi.org/10.1038/s41567-019-0774-3>.

Correspondence and requests for materials should be addressed to M.B.

Reprints and permissions information is available at www.nature.com/reprints.



Extended Data Fig. 1 | Fit results on the 2010 data of E07-007 and E08-025 experiments. The plots show the helicity-independent (black) and helicity-dependent (blue) photon electroproduction cross-sections off proton (circles) and neutron (squares) from¹⁷ and the data reported herein. The error bars correspond to the quadratic sum of the standard deviation statistical and systematic uncertainties on the cross-sections. The specific kinematics are indicated in each plot. Solid lines show the results of the HT fit described in this work, whereas the dashed lines (almost indistinguishable from the solid lines) show the results of the NLO fit.



Extended Data Fig. 2 | Fit results on the 2004 data of E00-110 and E03-106 experiments. The plots show the helicity-independent (black) and helicity-dependent (blue) photon electroproduction cross-sections off proton (points) and neutron (squares) from^{12,26}. The specific kinematics are indicated in each plot. Solid lines show the results of the HT fit described in this work, whereas the dashed lines (almost indistinguishable from the solid lines) show the results of the NLO fit. Neutron results in²⁶ only contain the amplitude of the DVCS-BH interference term and its standard deviation uncertainty. Data points in this figure for that experiment are placed along the calculated cross-section, but without any spread around it.